ZONAL MEAN CIRCULATION OBTAINED BY A NEWLY DEVELOPED MARTIAN ATMOSPHERIC GENERAL CIRCULATION MODEL.

Y. O. Takahashi (yosiyuki@pat.geophys.tohoku.ac.jp), H. Fujiwara, H. Fukunishi, *Department of Geophysics, Tohoku University, Japan*, **M. Odaka, Y.-Y. Hayashi,** *Division of Earth and Planetary Sciences, Hokkaido University, Japan*.

Introduction

We have newly developed a Mars General Circulation Model (GCM) to investigate basic global circulation characteristics of the Martian atmosphere. The topics we have investigated so far with this model are the north-south asymmetry of the meridional circulation and the role of topography in the cause of asymmetry [*Takahashi et al.*, 2002], and the migrating diurnal tide and its effect on the zonal mean circulation and dust transport. In this talk, we present the outline of our Martian GCM, and show briefly some of the basic characteristics of general circulation obtained by our model. As an example of the materials revealed by our model, the effect of the north-south surface elevation difference on the meridional circulation is described.

Model Description

The Martian atmospheric GCM presented here is based on the primitive equation system. The model upper boundary is at 9.3×10^{-7} hPa pressure level, which is located around 120 km altitude. The top boundary is placed at this altitude, since it has been recognized that a large vertical domain up to the upper middle atmosphere (~ 80 km altitude) is necessary to simulate the meridional circulation of the Martian atmosphere [e.g., *Wilson*, 1997]. Since the elevation difference of the Martian surface topography is large, following the way of constructing terrestrial atmospheric GCMs which include middle atmosphere, we employ $\sigma - p$ hybrid coordinate [e.g., *Arakawa and Lamb*, 1977]. The interface between the regions described by σ and p coordinates is 1.1 hPa pressure level.

The dynamical equations are solved by the spectral method in the horizontal direction, and by the finite difference scheme of *Arakawa and Suarez* [1983] in the vertical direction. The spectral truncation is triangular at wavenumber 10 (T10), which is roughly equivalent to a 11.25° × 11.25° latitude-longitude grid. The vertical domain is divided into 35 layers. The vertical grid interval increases with altitude up to the interface between σ and p coordinates; it is several hundred meters near the surface and a half of the scale height ($\sim$3–4 km) near the interface level. Above the interface level, the vertical grid interval is given by $\Delta \ln p/p_0 = 0.5$. The Leap frog scheme is used for the time integration and a second order time filter is adopted once every 20 time steps.

As for the radiative processes, the effects of CO_2 and dust suspended in the atmosphere are considered. As for the radiative effect of CO_2 the absorptions in the near infrared wavelength and CO_2 15 μm band are considered. The near infrared absorption is calculated by the simple analytical formula used by *Forget et al.* [1999]. The absorption of CO_2 15 μm band is evaluated by the following two schemes, since the model has very large vertical domain. Below the altitude of $\sim$80 km, the radiative transfer equation is solved numerically with the wavenumber averaged transmission function by correlated k-distribution method [e.g., *Liou*, 1992]. Above the altitude of $\sim$80 km, the parameterization by *Gordiets et al.* [1982] is adapted.

As for the radiative effect of dust the absorptions and scatterings in visible and infrared wavelengths are considered. The absorption and scattering in the visible wavelength are calculated by the two stream δ-Eddington radiative transfer equation. The absorption and scattering in the infrared wavelength are divided into the two wavelength regions according to the CO_2 15 μm band. The source function technique described in *Toon et al.* [1989] is used for the wavelength regions out of CO_2 15 μm band. The method of *Forget et al.* [1999] is used for the wavelength region of CO_2 15 μm band, The optical parameters of dust are obtained from *Ockert-Bell et al.* [1997] for visible wavelength, and from *Forget* [1998] for infrared wavelength.

The vertical mixing processes are the eddy mixing by turbulence and the convective adjustment. The eddy diffusion coefficients for momentum and heat are estimated by the *Mellor and Yamada* [1974, 1982] level 2 turbulence closure scheme. The eddy diffusion coefficient is diagnostically determined as a function of a Richardson number. In addition to this vertical diffusion, we incorporate convective adjustment for vertical mixing of thermal energy.

Rayleigh friction is imposed on the zonal wave component near the upper boundary. Time constant of the Rayleigh friction τ_{ray} is given as proportional to the square of pressure with $\tau_{ray} = 1/12$ sol at the upper boundary level.

The surface temperature is calculated from the heat budget equation of the ground surface and the thermal conduction equation of the subsurface soil. The subsurface domain is divided into 8 layers. The thermal conduction equation is solved with a centered difference scheme and is temporally integrated with Crank-Nicolson scheme.

The thermal and mass effect of CO_2 condensation and sublimation are considered. The change of atmospheric mass due to the formation of CO_2 ice polar cap is incorporated. The change of surface albedo associated with polar cap formation is also included. The CO_2 condensation/sublimation yields about 20-30 % variation of atmospheric total mass in the model.

Basic structure of zonal mean circulations

In Figure 1 and 2, we will demonstrate that our Mars GCM well represents general characteristics of the Martian atmospheric circulation which have been reported in the previous observational and GCM studies. Figure 1 shows the meridional cross sections of time- and zonal-mean circulation fields at the northern winter solstice ($L_s = 249° - 290°$) under the typical dust condition (visible dust optical depth of $\sim$0.3) from the ground up to the 2.0×10^{-4} hPa pressure level. Note that the contour interval is not constant but logarithmic in the panels of meridional wind and mass stream function (Figure 1a and b).

The meridional wind is southerly in almost all places except for the region near the ground surface. The returning flow in the surface mixed layer from the northern hemisphere to the southern hemisphere is mostly confined in the region near the ground up to $\sim$5 km altitude. The cross equatorial meridional circulation dominates in this season (Figure 1b). In the northern middle latitudes, an indirect cell forms. This indirect cell extends up to $\sim$ 60 km altitude.

Figure 1c shows the meridional distribution of zonal wind. In the northern winter hemisphere, the latitudinal width of the westerly jet is relatively narrow compared to that of the easterly jet. A wide region including most of the southern hemisphere and northern low latitudes is covered by easterly. The velocity of westerly jet reaches $\sim$ 120 m/s above 30 km altitude, while that of easterly jet increases slowly with height. Near the ground around 30° S, it is found to be westerly. The existence of the westerly near the ground in the southern hemisphere is verified by the atmospheric pressure observation by the radio occultation measurements of Mars Global Surveyor (MGS) [*Hinson et al.*, 1999].

As for the atmospheric temperature distribution, it is fairly uniform in the latitudinal direction below $\sim$20 km except for the northern winter high latitudes (Figure 1d). In the 20 km to 80 km altitudes, temperature increases from the equator to around 60° N. The increase of temperature toward the northern winter high latitudes has been observed by several spacecraft on Mars [e.g., *Santee and Crisp*, 1993; *Christensen et al.*, 1998].

Figure 2 is the same as Figure 1, except for the season, northern vernal equinox ($L_s = 343° - 15°$). The zonal mean fields show fairly symmetric structures with respect to the equator except for the low latitudinal region below $\sim$10 km altitude.

The meridional circulation is fairly symmetric with respect to the equator above $\sim$10 km altitude. In both hemispheres. the Hadley circulation extends to almost the same latitudes ($\sim 50° - 60°$). Indirect circulations are found in middle latitudes of both hemispheres. The intensity of the Hadley circulation is much weaker than that at northern winter solstice.

The zonal wind distribution becomes also fairly symmetric compared with that at northern winter solstice (Figure 2c). The velocities of westerly jets in both hemispheres are about 2/3 of the winter westerly jet. The flow is westerly at the equator around 20 km altitude. The equatorial westerly is observed also in the results of GCM experiments performed by *Haberle et al.* [1993] and *Forget et al.* [1999].

Corresponding to the zonal wind field, the temperature field shows fairly symmetric features (Figure 2d). As reported by observations and other GCM results [e.g., *Conrath et al.*, 2000; *Forget et al.*, 1999], there are mid- to high-latitude maximums of temperature above $\sim$20 km altitude in both hemispheres.

Topographically Induced North-South Asymmetry of the Meridional Circulation

In Figure 3, we show the seasonal variation of mass stream function under no dust condition (visible dust optical depth). Although the dust in the atmosphere has important impacts on the thermal structure and circulation of the Martian atmosphere, numerical experiments under no dust condition are useful. At northern summer solstice (Figure 3b) and northern winter solstice (Figure 3d), large cross-equatorial circulations form. However, as pointed out by *Haberle et al.* [1993] and *Wilson and Hamilton* [1996], the intensity of the cross-equatorial flow at northern summer solstice is found to be fairly weak compared with that at northern winter solstice. The important point is that the meridional circulation below $\sim$20 km altitude shows a fairly asymmetric pattern with respect to the equator during the equinox seasons (Figure 3a and c). That is, the intensity of northern circulation is stronger than that of southern circulation. Our previous work [*Takahashi et al.*, 2002] revealed that the difference in convective activity between northern and southern hemispheres cause these asymmetric circulations with respect to the equator. The difference of convective activity between the hemispheres is caused by the difference of surface potential temperature owing to the north-south elevation of the surface topography.

References

Arakawa, A., and V. R. Lamb, *Methods Comput. Phys.*, *17*, 173–265, 1977, Arakawa, A. and M. J. Suarez, *Mon.*
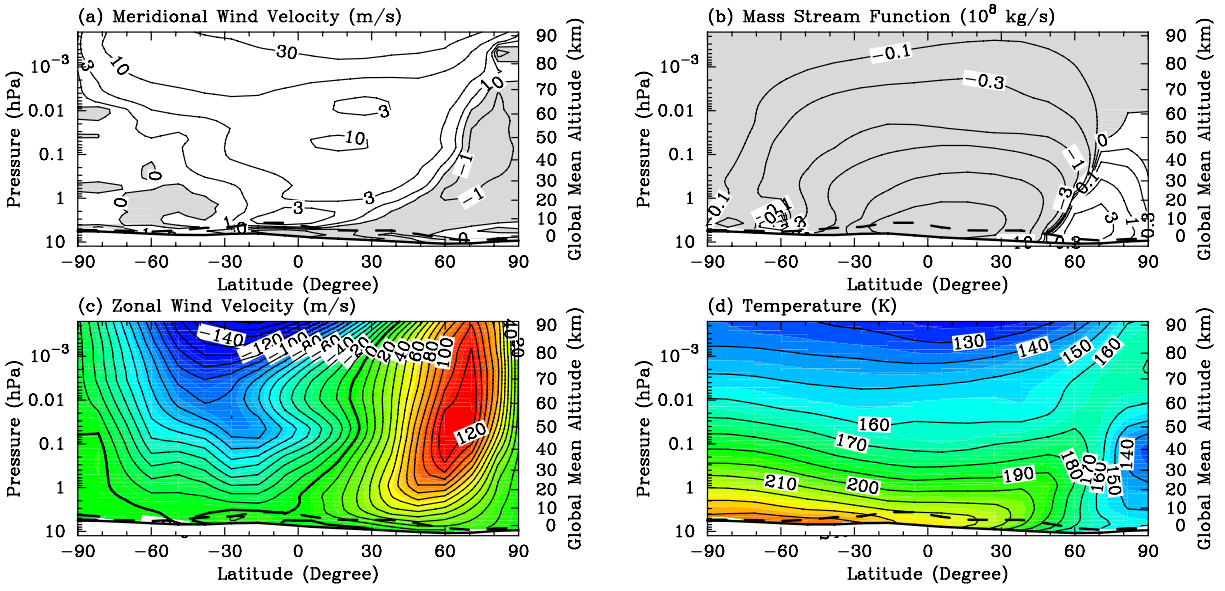
Figure 1: Time- and zonal-mean fields at the northern winter solstice ($L_s = 249° - 290°$) under the typical dust condition (visible dust optical depth of ~ 0.3) The vertical region from the ground up to $\sim 2.0 \times 10^{-4}$ hPa (~ 90 km altitude) is plotted. (a) meridional wind (m/s), (b) mass stream function (10^8 kg/s), (c) zonal wind (m/s), (d) temperature (K). Thick line drawn at ~ 6 hPa level indicates the zonal mean topography used in the model. Dashed line indicates the maximum extent of topography at each latitude. In panels (a) and (b), negative values are shaded. Note that contour intervals are logarithmic in panels (a) and (b).
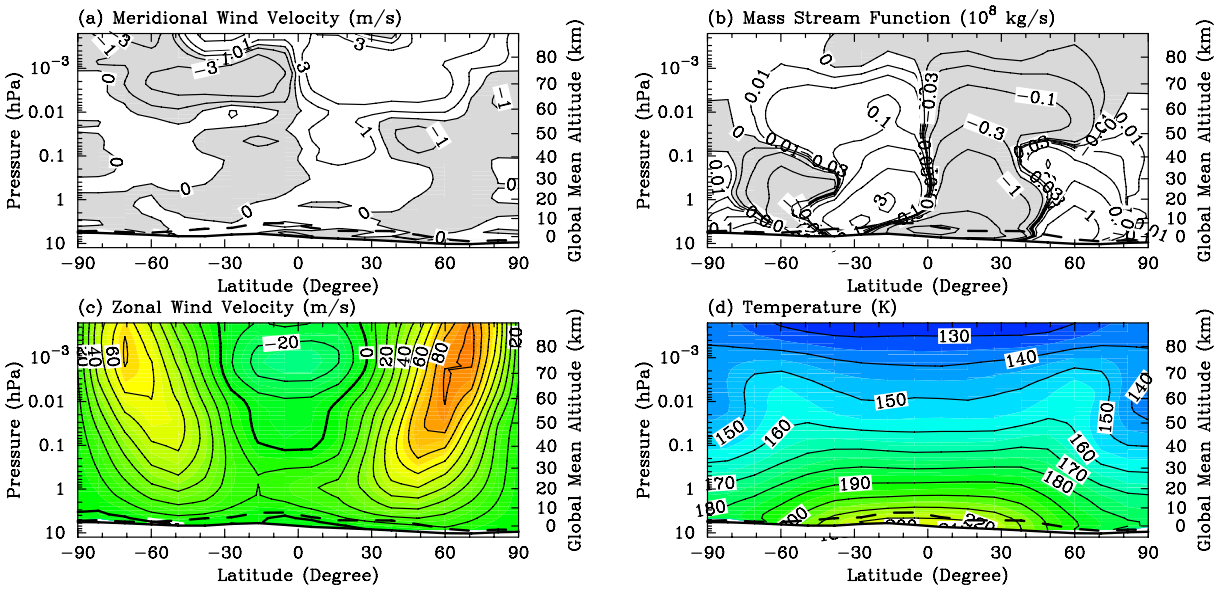
Figure 2: Same as Figure 1, except for the season, northern vernal equinox ($L_s = 343° - 15°$).

(a) Ls ~ 343° - 15°

(b) Ls ~ 75° - 104°

(c) Ls ~ 161° - 191°

(d) Ls ~ 249° - 290°
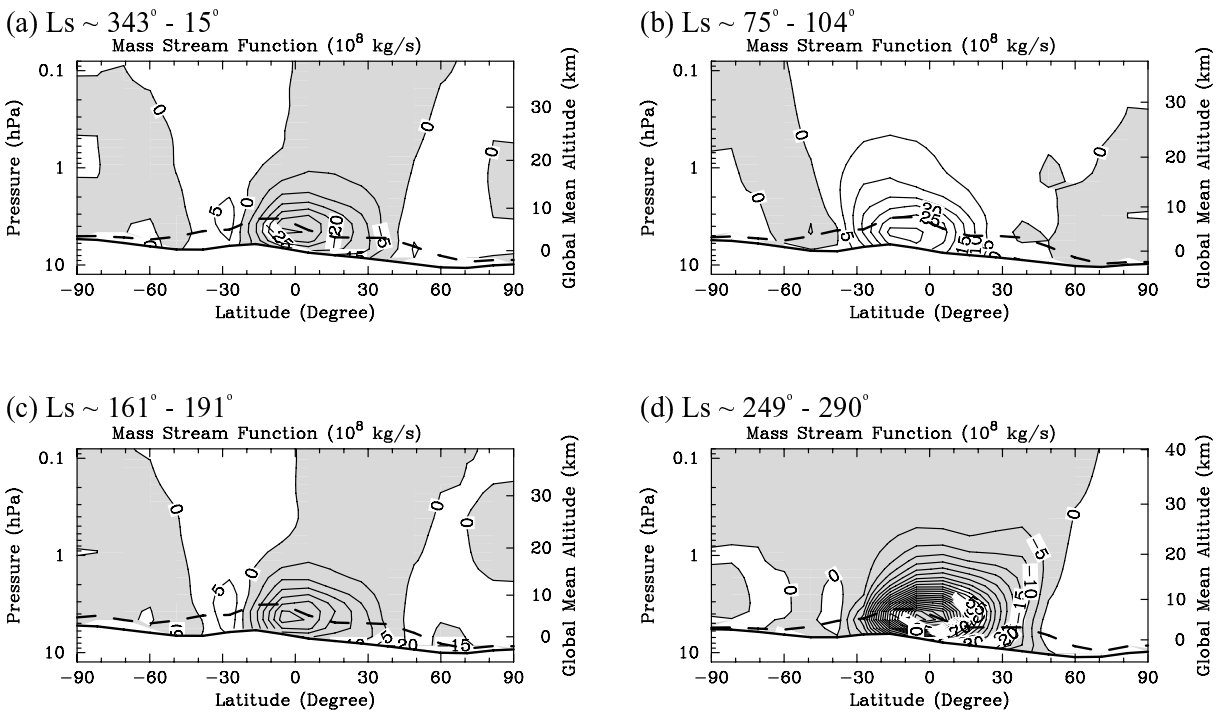
Figure 3: Seasonal variation of mass stream function under no dust condition (visible dust optical depth of 0) from the ground up to 1.0×10^{-1} hPa (~40 km altitude), (a) northern vernal equinox ($L_s = 343° - 15°$), (b) northern summer solstice ($L_s = 75° - 104°$), (c) northern autumnal equinox ($L_s = 161° - 191°$), and (d) northern winter solstice ($L_s = 249° - 290°$). Negative values are shaded. Note that contour intervals are constant and is 5×10^8 kg/s.

Wea. Rev., 111, 34–45, 1983, Christensen, P. R. et al., Science, 279, 1692–1698, 1998, Conrath, B. J. et al., J. Geophys. Res., 105, 9509–9519, 2000, Forget, F., Geophys. Res. Lett., 25, 1105–1108, 1998, Forget, F. et al., J. Geophys. Res., 104, 24155–24175, 1999, Gordiets, B. F. et al., J. Geophys. Res., 87, 4504–4514, 1982, Haberle, R. M. et al., C. B. Leovy, J. R. Murphy, H. Lee, and J. Schaeffer, J. Geophys. Res., 98, 3093–3123, 1993, Hinson, D. P. et al., J. Geophys. Res., 104, 26997–27012, 1999, Liou, K. N., Radiation and Cloud Processes in the Atmosphere, Oxford University Press, 1992, Mellor, G. L., and T. Yamada, J.

Atmos. Sci., 31, 1791–1806, 1974, Mellor, G. L., and T. Yamada, Rev. Geophys. Space Phys., 20, 851–875, 1982, Ockert-Bell, M. E. et al., J. Geophys. Res., 102, 9039–9050, 1997, Santee, M., and D. Crisp, J. Geophys. Res., 98, 3261–3279, 1993, Takahashi, Y. O. et al., Topographically Induced North-South Asymmetry of the Meridional Circulation in the Martian Atmosphere, J. Geophys. Res., in press, 2002, Toon, O. B. et al., J. Geophys. Res., 94, 16287–16301, 1989, Wilson, R. J., and K. Hamilton, J. Atmos. Sci., 53, 1290–1326, 1996, Wilson, R. J., Geophys. Res. Lett., 24, 123–126, 1997